Optimized design and flow physics of a wide operating range centrifugal compressor for automotive turbochargers

Seiichi Ibaraki[a,1] and Isao Tomita[a,2]

a Mitsubishi Heavy Industries, Ltd.,Nagasaki, 851-0392, Japan

Abstract: Turbocharger compressors impose a challenge to the designer when both a very wide operating range and high efficiency are required. The internal flow in a centrifugal compressor impeller is three dimensional and shows very complex flow phenomena, which makes the understanding of the loss generating mechanisms difficult and requires a considerable design effort to reach good performance. The design effort can however be reduced by applying an advanced design optimization system as an alternative to a conventional manual design based on the experience of the designer. In this study a centrifugal compressor impeller for an automotive turbocharger was designed by means of an aerodynamic design optimization system composed of an artificial neural network (ANN) and a genetic algorithm (GA). This resulted in two newly designed centrifugal compressor impellers. One has higher efficiency with slightly wider operating range compared to the baseline impeller. The other one has a twice as wide operating range compared to the baseline impeller with a minor decrease in efficiency. The difference between two optimized impellers was investigated both numerically and experimentally. It has been revealed that the circumferentially uniform blockage caused by the tip leakage vortex breakdown can suppress the occurrence of the rotating stall and extend the operating range.

Key Words: Centrifugal compressor; Optimized design; Artificial neural network; Genetic algorithm; Wide operating range; Vortex breakdown, Rotating stall

---

[1] E-mail: seiichi_ibaraki@mhi.co.jp, URL: https://www.mhi-global.com/
[2] E-mail: isao_tomita@mhi.co.jp, URL: https://www.mhi-global.com/

1 Introduction

Today turbocharging has become a fundamental technology to realize engine downsizing, which is an attractive strategy for low carbon emissions. High efficiency and wide operating range are strongly required for automotive turbochargers[1]. Especially centrifugal compressors for automotive turbochargers should operate with high efficiency from the surge limit to the choke limit. To increase the operating range of centrifugal compressors, recirculation bypass of the inducer is employed for some applications[2]. Also some devices such as variable inlet guide vanes[3] and low solidity diffusers[4] have been studied. However, all above countermeasures need extra cost and complexity of the turbocharging system.
Modern, high performance centrifugal compressor impellers demonstrate complex 3D blade geometries with a highly complex 3D flow[5]-[8]. The efficiency of centrifugal compressors has been improved over several decades by the progress of computational fluid dynamics and experimental fluid dynamics, which makes it increasingly more difficult to improve the efficiency further with reasonable stable operating range. Therefore, centrifugal compressor design can benefit largely from modern optimization techniques.
In this study two centrifugal compressor impellers for automotive turbochargers was designed by an aerodynamic design optimization system composed of an ANN and a GA. One has a higher efficiency with a slightly wider operating range compared to the baseline impeller. The other one has a twice as wide operating range compared to the baseline impeller with a minor decreased efficiency. Flow physics of the newly designed impellers has been investigated both experimentally and numerically. Especially the mechanism of significant increase of operating range has been studied in detail. In the results it has been revealed that the circumferentially uniform blockage caused by the tip leakage vortex breakdown suppress the occurrence of the rotating stall and increase the operating range. The tip leakage vortex breakdown plays a key role in map width enhancement.

2 Optimization strategy

2.1 Optimization procedure

Figure 1 shows the design procedure. The optimisation is driven by a GA in which the performance of each geometry is analysed by an ANN trained on the information contained in a database. Once the GA has found an optimum it is verified by a Navier-Stokes solver and is added to the database, resulting in a more accurate ANN. This procedure is repeated for a given number of iterations. A more complete description of the optimisation method can be found in published papers [9],[10].

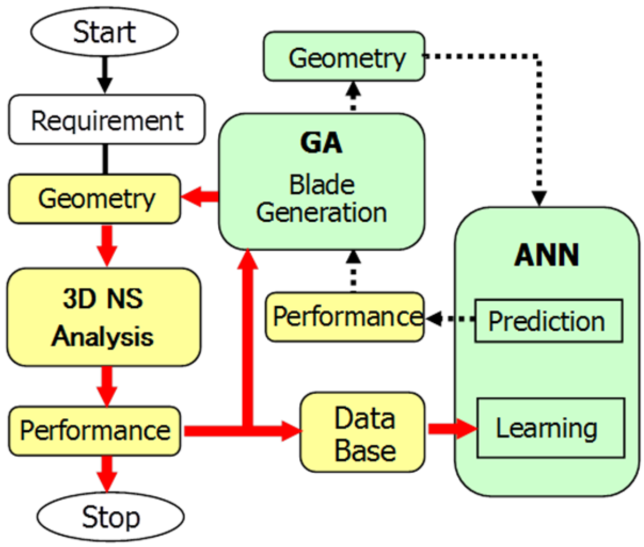

Figure 1: Optimization procefure

2.2 Boundary conditions and geometry definition

The design total to static pressure ratio of the compressor is 1.53. The atmospheric pressure is imposed as total inlet pressure, and the total inlet temperature is fixed at 293.15K. The inlet flow is axially oriented. At the outlet a static pressure is imposed corresponding to the required pressure ratio.
The impeller is backswept with splitter blades. The geometry is defined by the meridional contour and the camber line blade angles of the full and splitter blades at hub and shroud. The meridional contour definition is schematically shown in Figure 2(a), where subscript 0 denotes the leading edge of the blade and 3 denotes the trailing edge. The blade number is allowed to be changed in between minimum 4+4 and maximum 6+6.
The blade meridional contour at hub and shroud are defined by third-order Bézier curves with 4 control points, denoted by 0, 1, 2 and 3. The trailing edge diameter is set equal at hub and shroud. The trailing edge diameter is not a design variable but it is adjusted to compensate the variation in the blade trailing edge metal angle, which is a design variable. The diffuser exit diameter is fixed equal at the hub and at the shroud. The diffuser exit width is also fixed.
The camber line blade angle definition is achieved using third-order Bézier curves in the form of Bernstein polynomials as shown in Figure 2(b). The splitter blades are restricted to have the same trailing edge metal angle as the full blades. Same pitch at the hub and shroud is imposed at the trailing edge. The description of the blade is completed with the pre-specified thickness distribution. In total 27 design variables define the geometry.

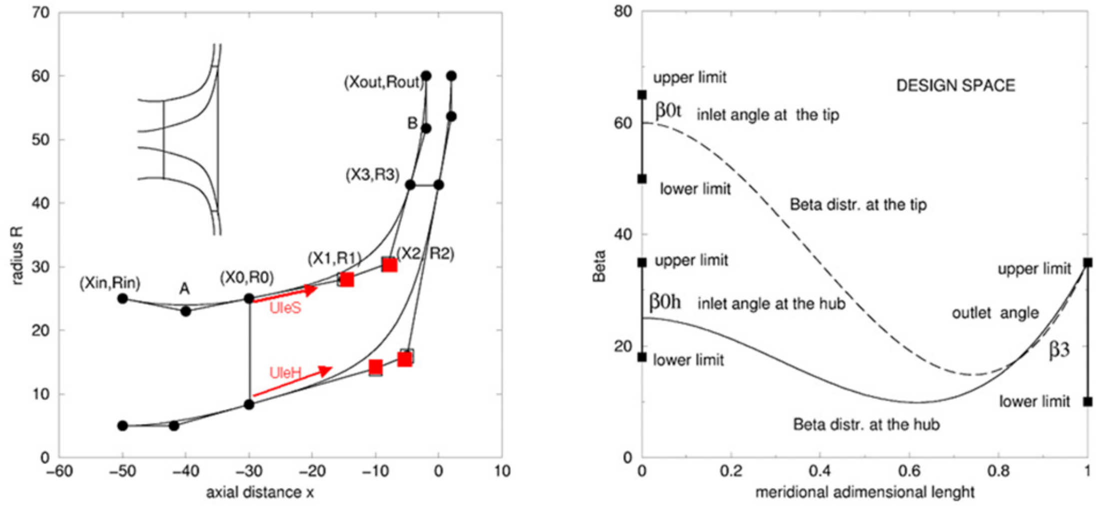

(a) Meridional contour definition

(b) Blade angle definition

Figure 2: Blade geometry definition

2.3 Objective functions

The GA is based on the evaluation of each individual's fitness, which is the inverse of the total penalty called the objective function. The penalties are associated with the Navier-Stokes analysis of the best individual proposed by the GA at the end of each optimization cycle. The ANN penalty is associated to each individual's performance predicted by the ANN during the optimization cycle. In both cases the penalty is formulated identically. The same performance vector is either predicted by the ANN or post-processed from the Navier-Stokes solution.

The vector of the 27 shape parameters constitutes the ANN input. The performance vector (as well the ANN output) from which the objective is computed, consists of the two mass flows divided by the splitter blade, the total-to-total efficiency, distortion and skew of the diffuser exit radial velocity profile, full blade and splitter blade Mach numbers and so on. The total performance vector has 165 elements. The total penalty is the sum of 9 objective functions as mass penalty, efficiency penalty, distortion-skew penalty, loading penalty, Mach number penalty and so on. More detailed information of the objective functions can be found in published papers [11].

3 Optimization results

Two optimized impellers were designed by the same optimization procedure. The only difference between both optimizations is the blade number limitation. In the first optimization (OPT1) the minimum blade number is 5+5. In the second optimization (OPT2) the minimum blade number is 4+4. The maximum blade number is 6+6 in both cases. Table 1 shows the

specifications of the optimum design compared to the baseline impeller. Figure 3 shows the optimum design impellers and the baseline impeller.
OPT1 has the blade number of 5+5 and larger inlet blade height and smaller exit blade width compared to the baseline impeller. OPT2 has the number of blades of 4+4 and slightly smaller inlet blade height. A remarkable feature of OPT2 is the forward inclined leading edge of the splitter blade.

Table 1: Specifications of optimum design impellers

	Optimized Impeller 1	Optimized Impeller 2	Baseline Impeller
Impeller diameter (mm)	50.0	49.6	49.0
Outlet width (mm)	4.14	3.75	4.20
Inlet tip diameter (mm)	39.5	37.1	37.8
Inlet hub diameter (mm)	13.9	12.6	12.6
Blade number	5+5	4+4	6+6

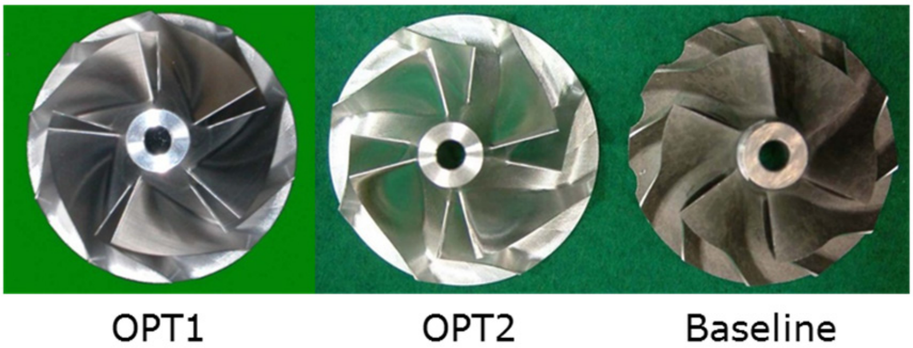

Figure 3: Optimum design impellers and baseline impeller

4 Performance test results and discussions

OPT1 and OPT2 have been further analysed both experimentally and numerically. Performance tests have been conducted using an automotive turbocharger. Each compressor volute has the same geometry, as well as same exit diameter of the vaneless diffuser. The compressor characteristics have been measured and compared with the baseline impeller.

4.1 Performance test results

Figure 4 shows the comparison of compressor characteristics of OPT1, OPT2 and the baseline impeller. The compressor total to total efficiency shown in Figure 4 is normalized by the peak efficiency of the baseline impeller. The flow rate is also normalized by the reference flow rate. OPT1 has a slightly higher efficiency and operating range compared to the baseline impeller. On the other hand OPT2 has a very wide operating range with a 1% decrease of peak efficiency.

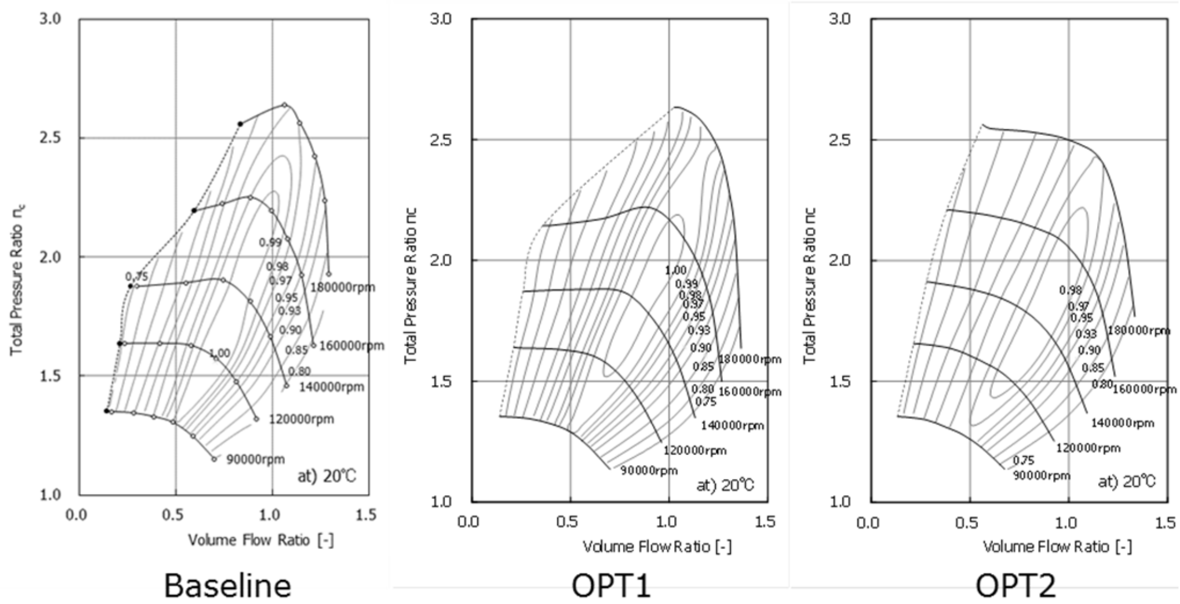

Figure 4: Comparison of compresor characteristics

Figure 5(a) shows the comparison of the peak efficiency for each rotational speed shown in Figure 4. Compared to the baseline OPT1 has a 0.5% higher peak efficiency around the total to total pressure ratio of 1.8 and more than 1.0% higher efficiency at pressure ratios above 2.2. On the other hand, OPT2 has about 1.0% lower efficiency compared to the baseline impeller.
In Figure 5(b) the operating range of the optimum designed impellers and the baseline impeller are compared. The operating range is defined as the flow range between maximum flow rate and surge limit at each rotational speed and normalized with the surge limit. The maximum flow late is defined as the flow rate at which the compressor efficiency drops below 65%. The horizontal axis of Figure 5(b) means the pressure ratio at surge limit at each rotational speed. The operating range of OPT1 is slightly smaller up to pressure ratio 1.9 compared to baseline impeller. However, the baseline impeller decreases its operating range rapidly at pressure ratios above 1.9. OPT1 does not have this rapid decrease of its operating range and remains a wide operating range up to a pressure ratio 2.5. OPT2 has almost equivalent operating range of the baseline impeller at the pressure ratio below 1.9 but a very wide operating range at pressure ratios beyond 1.9. OPT2’s operating range has more than doubled at the pressure ratio above 2.2 compared to the baseline impeller.

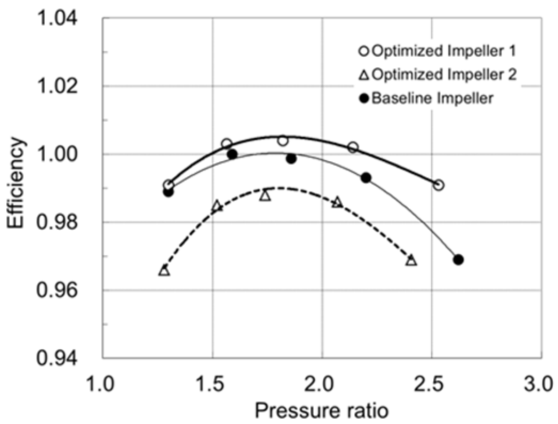

(a) Total to total efficiency

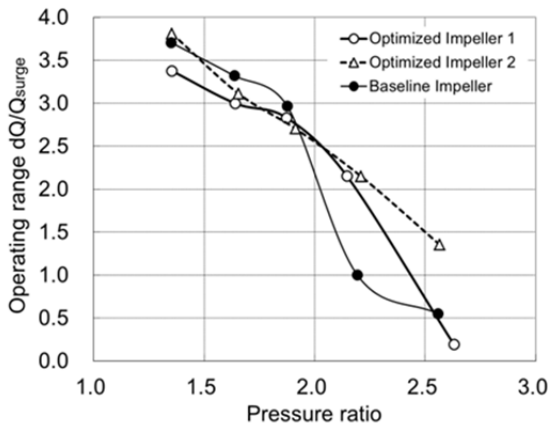

(b) Operating range

Figure 5: Comparison of compressor performance

4.2 Steady CFD results

The flow phenomena in the optimum designs have been investigated by detailed steady Navier-Stokes simulation. The commercial code ANSYS CFX ver.12 was used for this study. The whole domain of a compressor stage including the impeller, diffuser and volute has been calculated. The number of grid cells is about 2,470,000 for the impeller, 410,000 for the diffuser and 250,000 for the volute. A frozen rotor interface between the impeller outlet and the diffuser inlet has been applied. The k-ε model was used as the turbulence model. CFD was conducted at 160,000rpm and the flow rate near the peak efficiency condition.

In Figure 6 the limiting stream lines on the blade surface and the entropy distribution are compared. Also shown in Figure 6 are the identified vortex cores which are coloured with normalized helicity. Normalized helicity is defined as cosine of the angle made between the vortex vector and the velocity vector, and the domain where its absolute value is 1 indicates a strong rolling-up of a streamwise vortex.

From Figure 6(a), it is clear that the baseline impeller has a strong secondary flow rolling up from hub to shroud on the suction surface at the inducer. Because of this, low momentum fluids start to accumulate on the suction surface of the full blade near the end of the inducer. This low momentum fluids combined with the tip leakage flow accumulate and compose the high entropy region near the tip corner of the splitter blade pressure surface at the impeller exit. The strong secondary flow motion and tip leakage flow are the main causes of loss generation in the baseline impeller.

In contrast to the baseline impeller OPT1 does not have a remarkable secondary flow at the inducer as shown in Figure 6(b). Owing to this, the accumulation of low momentum fluid is suppressed near the tip corner of the splitter blade pressure surface at the impeller exit compared to the baseline impeller. Even though LE tip leakage vortex is much stronger due to the increased blade loading resulting from the smaller blade number, the area of highest loss region is much smaller than that of the baseline impeller because there is almost no accumulation of low momentum fluid by the secondary flow.

The internal flow phenomena and loss generation mechanisms of OPT2 are almost identical to those of OPT1. In contrast to OPT1, OPT2 has a secondary flow rolling up from mid-span to tip on the suction surface at the inducer as shown in Figure 6(c). Because of this secondary flow, the accumulation of the low momentum fluid on the full blade suction surface near the end of the inducer is observed. As a result, OPT2 has a relatively higher loss at the exit compared to OPT1.

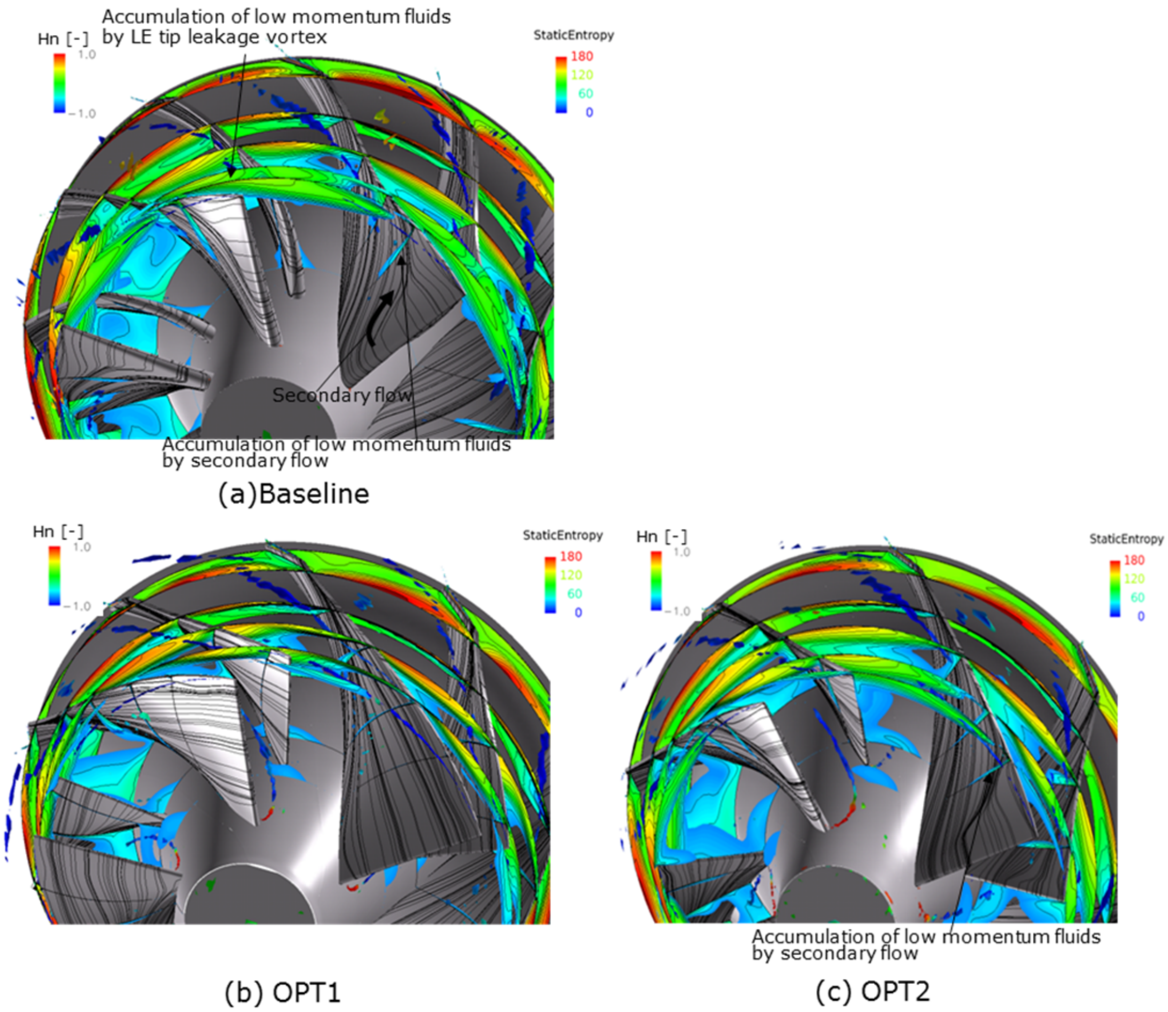

Figure 6: Comparison of limiting stream lines, vortex structure and entropy distribution

5 Pressure measurement results and discussions

5.1 Technique of measuring pressure fluctuations

To investigate the detailed unsteady flow phenomena, high-response pressure transducers were installed at positions 3 mm upstream from the impeller leading edge and 1.1 times the radius of the impeller, as shown in Figure 7. The transducers were installed at two positions along the circumference, and unstable phenomena were analysed via the time difference between the disturbances detected by each transducer. The blade passing frequency (BPF: speed N $\times$ number of blades Z (Hz)) is 26.7 kHz in the OPT1 and 21.6 kHz in the OPT2. Hence, the sampling frequency for the pressure fluctuation measurements was set at 1 MHz, and 35 or more points in a blade pitch between the full blade and splitter blade were measured. Near the surging (where the flow phenomena become unstable), the rotating stall phenomenon (in which a separated flow area rotates at a speed lower than that of the impeller) is known to occur. Therefore, to detect this, frequency fluctuations of 3 N (Hz) or lower were selected for a low-pass filter.

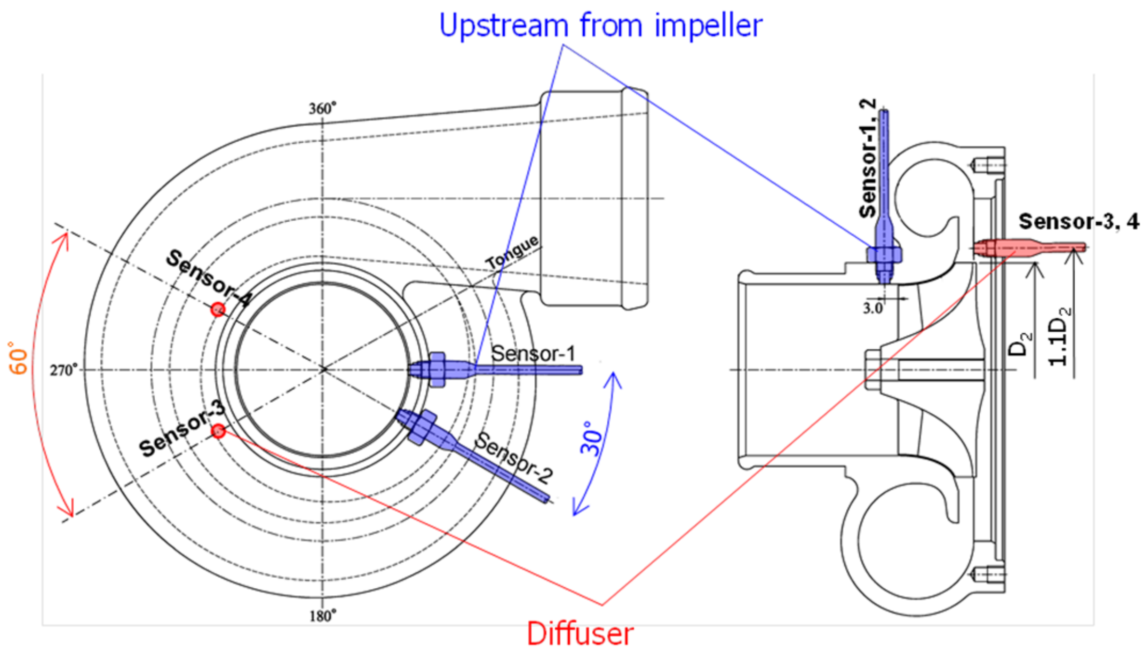

Figure 7: Pressure fluctuation measuring positions

5.2 Pressure measurement results

Figure 8 shows the results of the pressure fluctuation measurements in the OPT1. Figure 8(a) shows the results at the peak pressure point. The pressure wave fluctuation of the impeller was plotted over a 0.25 ms interval, corresponding to 0.7 of the impeller rotation. The pressure fluctuation caused by blade passing was clearly detected, and the pressure wave of each blade had the same shape. The waveform in the low-pass filter was plotted over 5 ms, corresponding to 13 rotations of the impeller. At this operating point, low-frequency phenomena such as rotating stall were not detected. In the pressure fluctuation wave of the diffuser, no significant phenomena other than the passing of full blades and splitter blades were observed. Figure 8(b) shows the pressure fluctuation waves at the small flow rate point. The low-pass filter wave of the impeller exhibited low-frequency instability. Moreover, at the diffuser, pressure fluctuations corresponding to full blades and splitter blade passage were indistinguishable, and unstable phenomena were assumed to affect the diffuser.

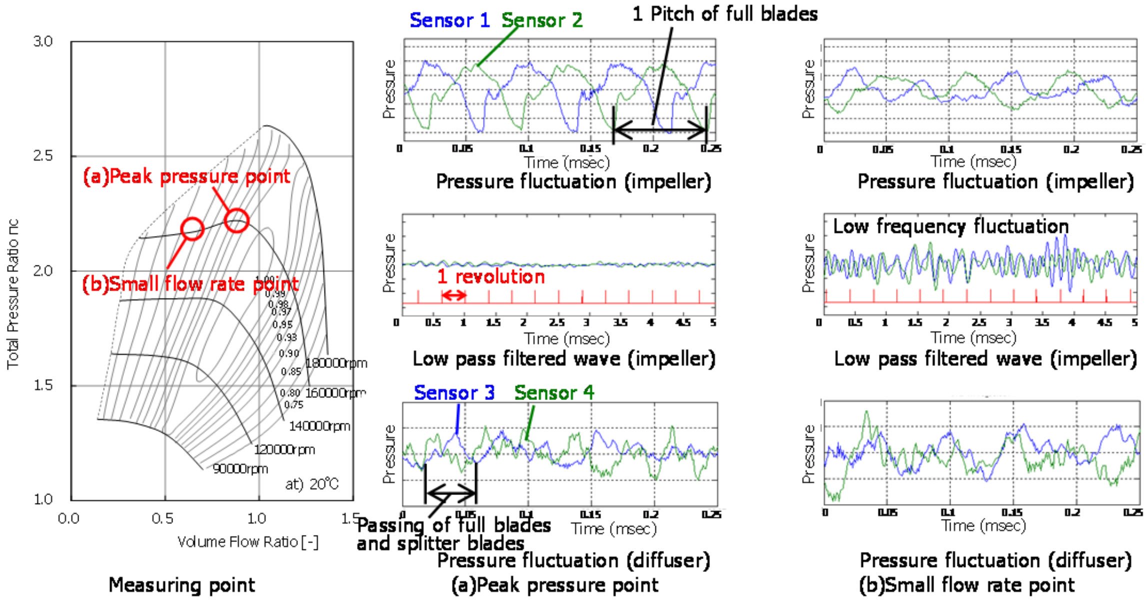

Figure 8: Results of pressure fluctuation measurements (OPT1)

Figure 9 shows detailed analysis results from the impeller low-pass filter at the small flow rate point. Transducers 1 and 2 were separated by a 30 degrees, and the time interval of the low frequency disturbance detected at transducer 1 and transducer 2 was 0.05 ms. The disturbance therefore required 0.05 ms × 360degrees / 30degrees = 0.60 ms to cover 360deg. In the actual measurements, a similar disturbance was detected by transducer 1 after 0.60 ms. The time required for one complete impeller rotation was 0.375 ms. Thus, the rotational speed of the disturbance was approximately 63% of the impeller speed. Moreover, three disturbances were simultaneously detected. This phenomenon is the same as a rotating stall with separated flow areas on the impeller blades, and each disturbance was presumed to be a rotating stall cell. However, it differed from a normal rotating stall. Some very unstable behaviours, such as temporal changes of stall cell number from two to four, were observed.

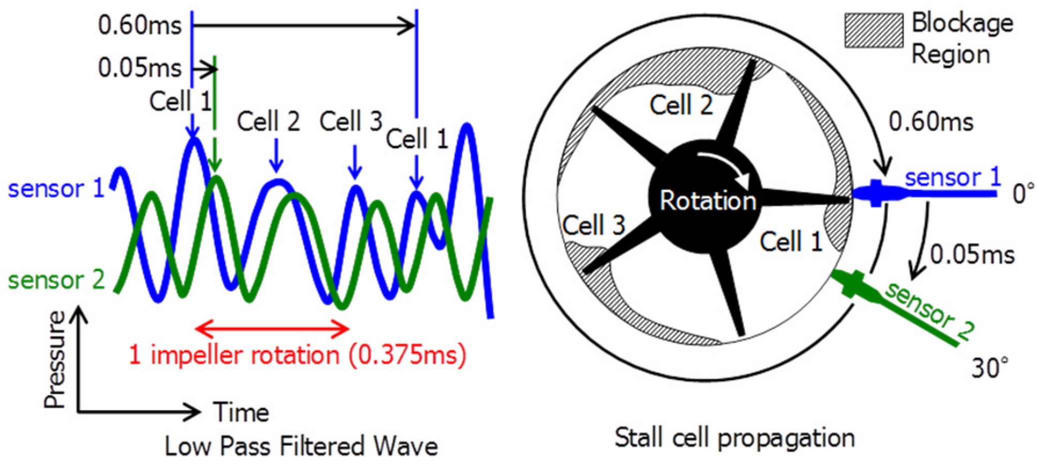

Figure 9: Structure of a rotating stall (OPT1)

The pressure fluctuation measurement results for the OPT2 are shown in Figure 10. At the peak efficiency point, shown in Figure 10(a), a low-frequency fluctuation was not observed. At the small flow rate point, a slight low-frequency fluctuation was observed in the low-pass filter wave-form. However, the fluctuation was contained within several rotations, and no significant phenomenon was evident. Also, full blades and splitter blades could be distinguished at the diffuser, and the flow phenomena were assumed to be uniform.

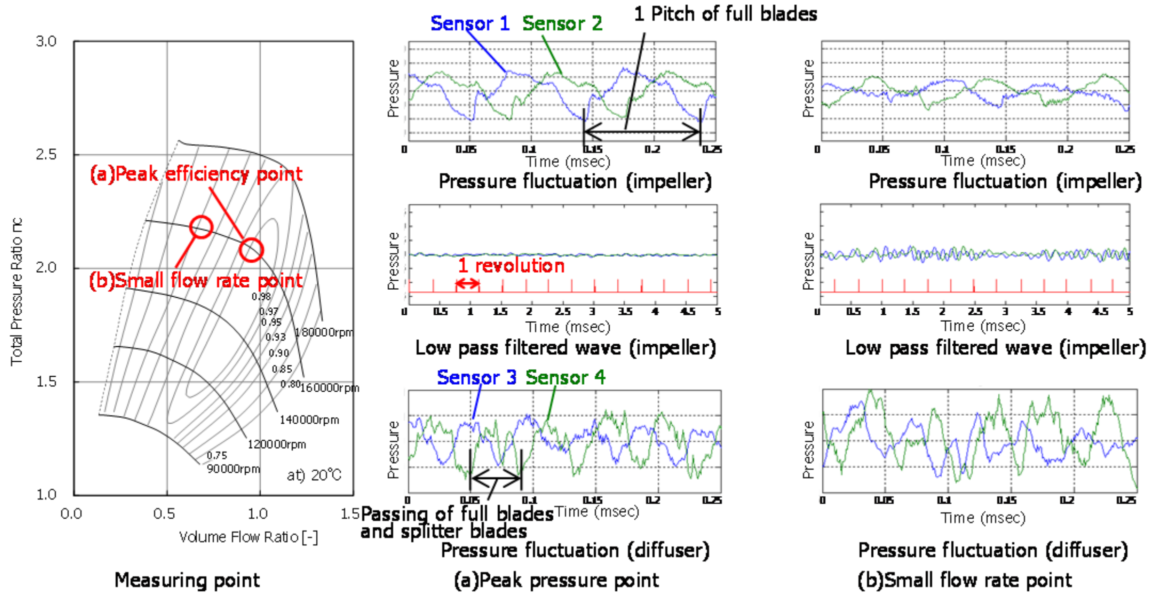

Figure 10: Results of pressure fluctuation measurements (OPT2)

5.3 Unsteady steady CFD results

The unsteady flow analysis was conducted under the same operational conditions as the pressure fluctuation measurements. The same way as steady CFD described in section 4.2, ANSYS CFX ver.12 was used with same turbulence model, computational domain and number of grids. Time steps per iteration ware 0.00375 ms for OPT1 and 0.0075 ms for OPT2, corresponding to 20 steps and 12.5 steps for one full blade pitch respectively. Figure 11 compares the calculated and measured results for the pressure ratio. Although the absolute values showed slight differences, the pressure-flow characteristics of the OPT1 and OPT2 were well simulated.

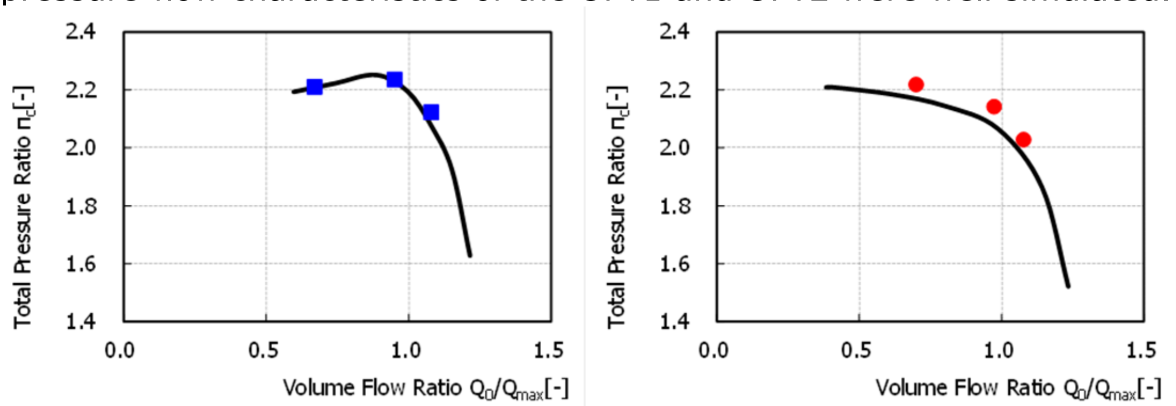

(a) OPT1 (b) OPT2

Figure 11: Verification of numerical analysis

Figure 12 shows the three-dimensional vortex structure coloured with normalized helicity and stream lines on the blade. The figure shows the generation of a tornado-shaped vortex on the blades of the OPT1. Its movement between blades is as follows. The mainstream avoids the vortex on the suction surface of the splitter blade, and the attack angle (the difference between the flow angle and the blade angle) becomes large at t = 0.0 ms. Flow separation is observed on the next blade at t = 0.049 ms, and the separated flow rises as a tornado-shaped vortex at t = 0.090 ms. Each vortex moves over the impeller in this way, while the number of vortices changes temporally, as the measurements indicate. This type of vortex is the main generator of a rotating stall cell[12]-[15], and it is thought that the circumferential expansion of these cells with decreasing flow rate is what triggers surging.
The internal flow structure of the OPT2 is shown in Figure 13. In the OPT2, the leakage flow between the blade tip and the blade casing forms a tip leakage vortex. This type of vortex cannot maintain a longitudinal shape via its own rotation and the adverse pressure gradient in the impeller. Hence, vortex breakdown occurs, and the vortex dissipates in a spiral flow. The dissipated leakage vortex forms a uniform stall layer in the circumferential direction at the blade tip ends.

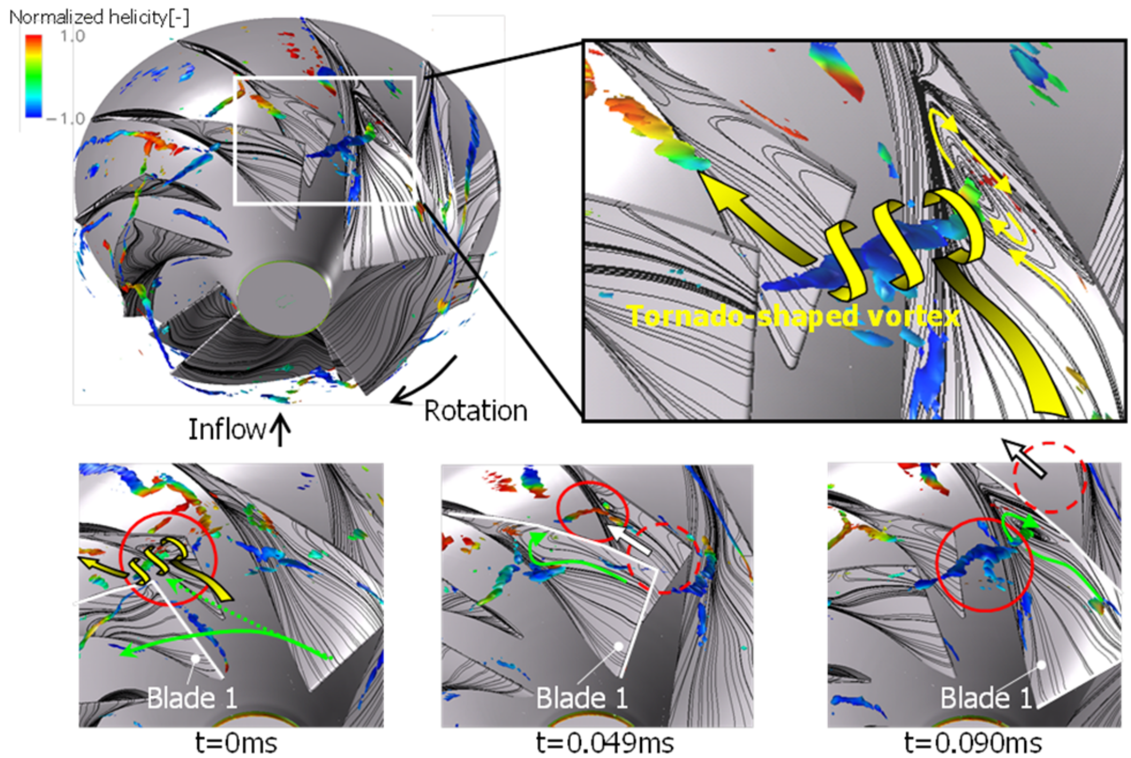

Figure 12: Internal flow structure (small flow rate point in a OPT1)

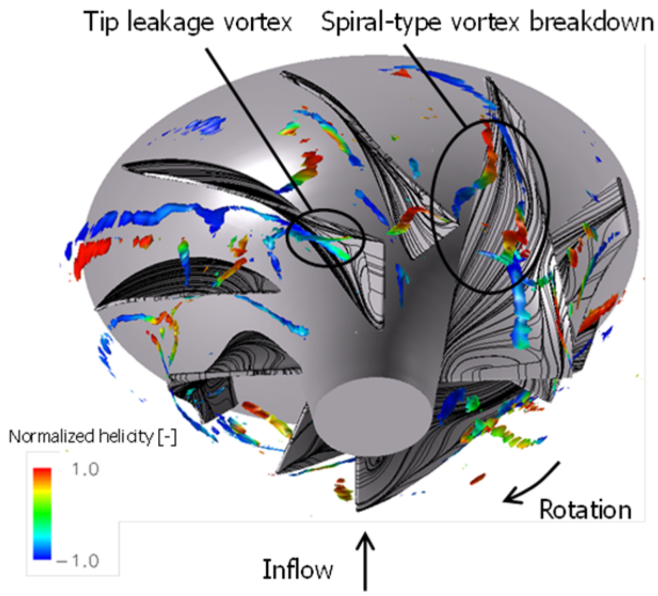

Figure 13: Internal flow structure (small flow rate point in a OPT2)

Figure 14 shows an image of the flow structure at the small flow rate point. In the OPT1, a rotating stall cell is generated by the tornado-shaped vortex and its accompanying stall area. In the OPT2, the flow is stabilized by creating a uniform thin stall area at the tip of the blades, and this is accomplished by controlling the local tip leakage vortices. The stall area created by the dissipated leakage flow becomes uniformly thick as the flow rate decreases, and contributes to flow stabilization near the surging. On the other hand, reduction of efficiency is controlled by eliminating the stall area at the high flow rate operating point.

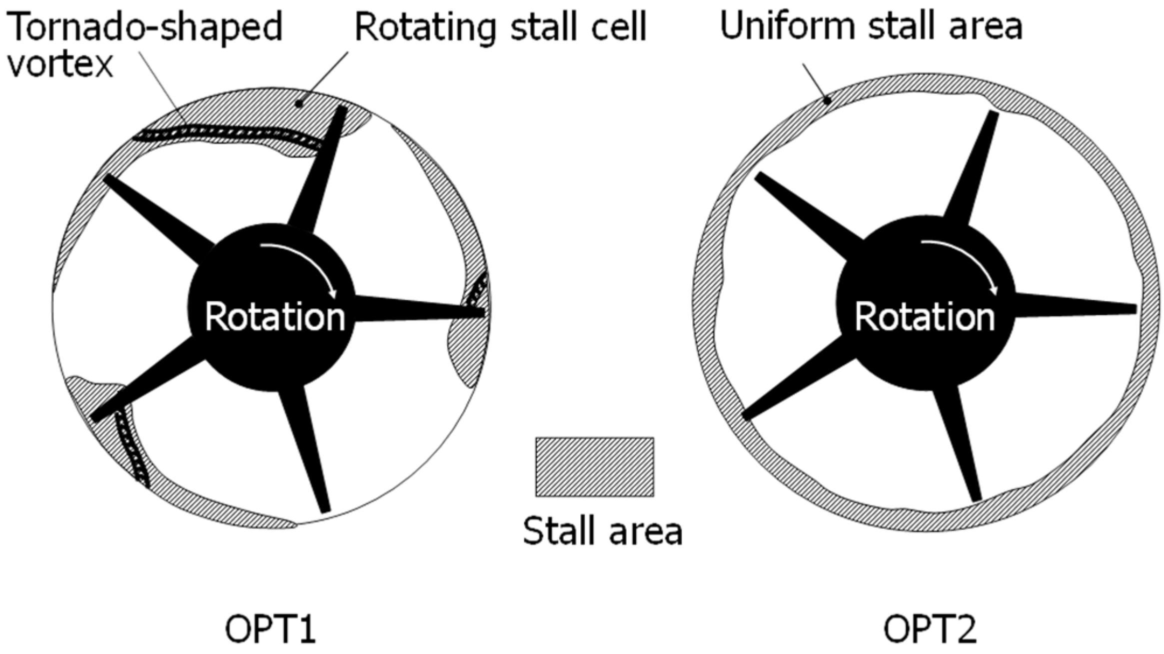

Figure 14: Images of flow structure

6 Summary and Outlook

In this study an advanced optimized design system composed of an ANN and a GA alternative to a conventional design system has been applied to design two optimized impellers of OPT1 and OPT2. Their performance and flow physics have been investigated experimentally and numerically. The following conclusions are obtained.

(1) OPT1 has a higher efficiency with slightly wider operating range compared to the baseline impeller. OPT2 has a twice as wide operating range compared to the baseline impeller with a minor decrease in efficiency. This successful result clearly demonstrates the benefits of advanced optimization systems composed of an ANN and a GA.

(2) OPT1 has a 0.5% higher peak efficiency at pressure ratio 1.8 and more than 1.0% higher efficiency above pressure ratio 2.2 compared to the baseline impeller. OPT1 has a very smooth flow without pronounced secondary flow at the inducer and thus achieves a higher efficiency compared to the baseline impeller.

(3) OPT2's operating range has increased more than double at the pressure ratio above 2.2 with almost equivalent operating range at low pressure ratio and 1% lower efficiency compared to the baseline impeller. Owing to a slightly stronger secondary flow compared to OPT1, OPT2 has lower efficiency.

(4) As flow rate is decreased, OPT1 encounters the rotating stall triggered by the flow separation with the tornado-shape vortex. On the other hand OPT2 provides the circumferentially uniform blockage near tip region caused by the tip leakage vortex breakdown. Owing to this, occurrence of the rotating stall is suppressed and a significant increase of operating range is achieved.

References

[1] Osako, K., Jinnai, Y. Samata, A., Suzuki, H., Ibaraki, S., Hayashi, N., 2006, " Development of the High Performance and High Reliability VG Turbocharger for Automotive Applications", MHI Technical Review, Vol. 43, No. 3.

[2] Fisher, F. B., 1988, "Application of Map Width Enhancement Devices to Turbocharger Compressor Stages", SAE Paper 880794.

[3] Tomita, I., An, B. And Nanbu, T., 2014, "A New Operationg Range Enhancement Device Combined with a Casing Treatment and Inlet Guide Vanes for Centrifugal Compressor", IMecE, 11th International Conference on turbochargers and turbocharging.

[4] Ibaraki, S., Ogita, H. and Yamada, T., 2007, " Development of a Wide Operating Range Turbocharger Compressor with a Low Solidity Vaned Diffuser", CIMAC No. 166.

[5] Ibaraki, S., Higashimori, H. and Mikogami, T., 1998, "Flow Investigation of a Centrifugal Compressor for Automotive Turbochargers", SAE Paper 98-P94.

[6] Ibaraki, S., Higashimori, H. and Matsuo, T., 2001, "Flow Investigation of a Transonic Centrifugal Compressor for Turbocharger", 23rd CIMAC.

[7] Ibaraki, S., Matsuo, T., Kuma, H., Sumida, K and Suita, T., 2003, " Aerodynamics of a Transonic Centrifugal Compressor Impeller" , ASME Journal of Turbomachinery, Vol.125, No.2, pp. 346-351.

[8] Ibaraki, S., Furukawa, M., Iwakiri, K. and Takahashi, K., 2001, " Vortical Flow Structure and Loss Generation Process in a Transonic Centrifugal Compressor Impeller", ASME Paper No. GT2007-27791.

[9] Pierret S. and Van den Braembussche R.A., 1998, "Turbomachinery blade design using a Navier-Stokes solver and Artificial Neural Net-

work", ASME Trans. Journal of Turbomachinery, Vol. 121, No. 9, (pp. 326-332).

[10] Alsalihi Z. and Van den Braembussche R.A., 2002, "Evaluation of a Design Method for Radial Impellers Based on Artificial Neural Network and Genetic Algorithm", ASME ESDA 2002/ATF-069, Istanbul.

[11] Ibaraki, S,. Van den Braembussche, R., Verstraete, T., Subimoto, K. And Tomita, I., 2014, "Aerodynamic Design Optimization of a Centrifugal Compressor Impeller Based on an Artificial Neural Network and Genetic Algorithm", IMecE, 11th International Conference on turbochargers and turbocharging.

[12] Inoue, M., Kuroumaru, M., Tanino, T., and Furukawa, M., 2000, "Propagation of Multiple Short Length-Scale Stall Cells in an Axial Compressor Rotor," Trans. ASME, Journal of Turbomachinery, Vol.122, pp.45-54.

[13] Yamada, K., Furukawa, M., and Inoue, M., 2002, "Numerical Analysis of Rotating Stall Inception in an Axial Compressor Rotor," Proceedings of the 5th JSME-KSME Fluids Engineering Conference.

[14] Yamada, K., Furukawa, M., Fukushima, H., Ibaraki, S., Tomita, I., 2011, "The Role of Tip Leakage Vortex Breakdown in Flow Fields and Aerodynamic Characteristics of Transonic Centrifugal Compressor Impellers", ASME Paper, GT2011-46253.

[15] Tomita, I., Ibaraki, S., Furukawa, M., Yamada, K., 2012, "The Effect of Tip Leakage Vortex for Operating Range Enhancement of Centrifugal Compressor", ASME Paper, GT2012-68947.